





Nanofabrication of plasmon-tunable nanoantennas for tip-enhanced Raman spectroscopy

Cite as: J. Chem. Phys. **153**, 114201 (2020); <https://doi.org/10.1063/5.0021560>

Submitted: 12 July 2020 . Accepted: 28 August 2020 . Published Online: 17 September 2020

Bruno S. Oliveira, Bráulio S. Archanjo , Rogério Valaski, Carlos A. Achete , Luiz Gustavo Caçado , Ado Jorio , and Thiago L. Vasconcelos 



View Online



Export Citation



CrossMark

Lock-in Amplifiers
up to 600 MHz



Watch



Nanofabrication of plasmon-tunable nanoantennas for tip-enhanced Raman spectroscopy

Cite as: J. Chem. Phys. 153, 114201 (2020); doi: 10.1063/5.0021560

Submitted: 12 July 2020 • Accepted: 28 August 2020 •

Published Online: 17 September 2020



View Online



Export Citation



CrossMark

Bruno S. Oliveira,¹ Bráulio S. Archanjo,¹ Rogério Valaski,¹ Carlos A. Achete,¹ Luiz Gustavo Cançado,² Ado Jorio,³ and Thiago L. Vasconcelos^{1,a)}

AFFILIATIONS

¹Divisão de Metrologia de Materiais, Instituto Nacional de Metrologia, Qualidade e Tecnologia (Inmetro), Duque de Caxias, RJ 25250-020, Brazil

²Departamento de Física, Universidade Federal de Minas Gerais, Belo Horizonte, MG 30270-901, Brazil

³Electrical Engineering and Innovation Technology Graduate Programs, Universidade Federal de Minas Gerais, Belo Horizonte, MG 30270-901, Brazil

Note: This paper is part of the JCP Special Topic on Spectroscopy and Microscopy of Plasmonic Systems.

a) Author to whom correspondence should be addressed: tlvasconcelos@inmetro.gov.br

ABSTRACT

Plasmon-tunable tip pyramids (PTTPs) are reproducible and efficient nanoantennas for tip-enhanced Raman spectroscopy (TERS). Their fabrication method is based on template stripping of a segmented gold pyramid with a size-adjustable nanopyramid end, which is capable of supporting monopole localized surface plasmon resonance (LSPR) modes leading to high spectral enhancement when its resonance energy is matched with the excitation laser energy. Here, we describe in detail the PTTP fabrication method and report a statistical analysis based on 530 PTTPs' and 185 ordinary gold micropylramids' templates. Our results indicate that the PTTP method generates probes with an apex diameter smaller than 30 nm on 92.4% of the batch, which is a parameter directly related to the achievable TERS spatial resolution. Moreover, the PTTPs' nanopyramid edge size L , a critical parameter for LSPR spectral tuning, shows variability typically smaller than 12.5%. The PTTP's performance was tested in TERS experiments performed on graphene, and the results show a spectral enhancement of up to 72-fold, which is at least one order of magnitude higher than that typically achieved with gold micropylramids. Imaging resolution is in the order of 20 nm.

Published under license by AIP Publishing. <https://doi.org/10.1063/5.0021560>

I. INTRODUCTION

Optical nanoantennas are the main objects that give tip-enhanced Raman spectroscopy (TERS) the ability to overcome the optical diffraction limit ($\approx \lambda/2$) by extracting the near-field information to generate high resolution Raman images.^{1–9} They are defined as devices capable of converting the propagating optical radiation into localized energy and vice versa,^{4,10–12} resulting in local spectral enhancement with spatial resolution ranging from tens of nanometers down to below 1 nm, depending on the technical approach.¹³ Considering our geometry of interest here, which is the simplest tip-only TERS configuration working roughly 5 nm distance from

the sample, the resolution is dictated by the nanoantenna's apex diameter.^{14–22} In this case, although the two important properties that define the quality of a TERS probe, i.e., its optical efficiency and apex size, are well established, a large-scale batch production of high quality TERS probes with high reproducibility is yet challenging.^{11,16,23} While different methods to make tips, such as electrochemical etching of gold wire and metallic covering of commercially available Si or Si₃N₄ cantilever probes, have served the TERS practitioners for many years, significantly advancing the technique,²⁴ low-reproducibility in the probe morphology or relatively poor optical efficiency is still frequently an issue that limits the overspread of the technique beyond highly experienced groups. Special concern can be

stressed when utilizing TERS to study two-dimensional (2D) samples that demand comparatively higher optical efficiencies because, differently from the case of molecules, where spectral enhancement (ratio between TERS and confocal intensities, $I_{\text{TERS}}/I_{\text{confocal}}$) higher than 10 is not unusual,²⁵ in 2D, the near-field signal competes with the far-field information coming from a considerably larger area.^{7,12,24,26–36}

Addressing the fabrication reproducibility on the probe's morphology, Johnson *et al.* reported a remarkable improvement by applying template stripped gold micropyramids as TERS probes.³⁷ The method is compatible with large-scale batch production and is inspired by the previously reported method of using pyramidal-like cavities microfabricated on Si wafers as templates for hollow gold micropyramids production.^{38–40} According to Ref. 37, this method leads to TERS probes with an apex diameter of 20 nm with high yield. On the other hand, since the micropyramid does not present any nanostructured surface features or discontinuation close to its apex, it is not designed to support localized surface plasmon resonance (LSPR) and, therefore, only generates moderate field enhancements based solely on the lighting-rod effect.^{12,41}

Previously, we reported the fabrication of plasmon-tunable tip pyramids (PTTPs) based on a modified template-stripping fabrication technique.⁴¹ The PTTPs are optical nanoantennas consisting of two main structures that compose the final shape of the TERS probe: a gold pyramidal frustum with a square base with a gold nanopyramid sitting on the center of its smaller base plateau (see Fig. 1). The edges of the plateau are sized to $\sim 1 \mu\text{m}$, whereas the nanopyramid has a lateral size L that can be in between 300 nm and 700 nm, to adjust the LSPR mode energy to match incident laser wavelengths in the optical and near IR ranges.^{41,42} Because of its unique structure, the PTTPs support monopole LSPR modes, where the plateau serves as an electronic reservoir, as demonstrated by theoretical simulations.⁴³ The highest field enhancement occurs for the matching of the second monopole mode ($L = 3/4 \lambda_{\text{eff}}$) with the incident laser wavelength ($\lambda_{\text{laser}} = 632.8 \text{ nm}$ in our case),⁴³ leading to TERS spectral enhancements of orders of magnitude higher than those produced by a gold micropyramid.⁴¹ This condition is satisfied when the nanopyramid edge size is set to $L \approx 470 \text{ nm}$.^{12,41} PTTPs have been successfully applied on TERS experiments for the investigation of single layer graphene on a glass substrate⁴¹ and gold nanoparticles,⁴⁴

graphene nanoflakes,^{33,36} GaS,³⁵ single-wall carbon nanotubes,⁴¹ and low-angle twisted bilayer graphene.⁴⁵

In this work, we present details about the PTTP fabrication method and report the metrological characterization of PTTPs and gold micropyramids. We show that the innovative PTTP not just has a favorable structure to support monopole LSPR modes leading to unprecedented spectral enhancements but it is also fabricated by a reproducible method compatible with large-scale production. Based on a statistical analysis of the data from 715 pyramidal cavities, we show that the PTTP fabrication method yields probes with an apex diameter smaller than 30 nm in 92.4% of the batch, an improvement of 210% when compared with the conventional micropyramid method.

II. TECHNICAL DETAILS

A. PTTP morphology and previous results

The PTTP, as shown in Fig. 1, was introduced in Ref. 41, where its optical and morphological properties were characterized using scanning transmission electron microscopy, electron energy loss spectroscopy (EELS), and computational simulations. In Ref. 43, its optical and morphological properties were linked by theoretical simulations. TERS results using the PTTP probes on 2D samples can be found in Refs. 12, 33, 35, 36, 41, and 43–45, which sum up to more than 20 TERS experiments with different tips.

B. Nanofabrication and characterization

The template stripped method employed to fabricate pyramidal-like TERS probes is based on two major key factors: the anisotropic etching of Si with KOH aqueous solution, which reveals the {111} planes of the Si crystal as pyramidal-like cavities,^{46–48} and the poor adhesion of gold to the Si or SiO₂ substrate.³⁹ These features allow the fabrication of re-usable cavities on Si wafers as templates for the hollow gold micropyramid or PTTP structures.

The starting material is a p-type Si wafer {100} with a 1 μm thick SiO₂ cover layer [Fig. 2(a)].⁴⁹ The fabrication method begins with a lithography process to expose Si on disk-shaped areas of 25 μm diameter [Fig. 2(b)]. We used focused ion beam (FIB) in a dual beam microscope (FEI Nova NanoLab 600) to perform ion beam lithography. Light lithography could also be employed in this step without loss of quality or control. The FIB parameters used were 30 kV of accelerating voltage and ion beam current of 20 nA. The remaining SiO₂ cover layer works as a protective mask against undesirable substrate etching. An anisotropic etching is performed by submerging the substrate in an aqueous solution of KOH and isopropyl alcohol at a concentration of 6:3:1 wt./wt. (H₂O:KOH:IPA). The temperature control of the anisotropic etching is a critical parameter and must be carefully stabilized at 65 °C. In this condition, the anisotropy of the process is improved, leading to an etching rate along the Si [100] direction hundreds of times higher than that along the [111] direction. This results in a pyramidal-like cavity with Si {111} plane faces and a square bottom made of Si {100} [Fig. 2(c)]. This square bottom is diminished, and the cavity goes deeper while the etching proceeds. If not stopped, the anisotropic etching results in a complete pyramidal cavity.

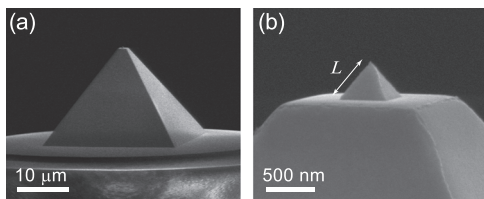


FIG. 1. Scanning electron microscopy images of a PTTP nanoantenna already mounted to perform as a TERS probe. (a) An open view of the whole PTTP's structure fixed at the top of a tuning fork with epoxy resin. (b) A higher magnification image of the PTTP's end portion, where the nanopyramid is seen centered on the plateau area. The white double-arrow line in (b) indicates the nanopyramid edge size L . All four nanopyramid faces are composed of equilateral triangles, and therefore, all edges, including the base ones, have the same length L .

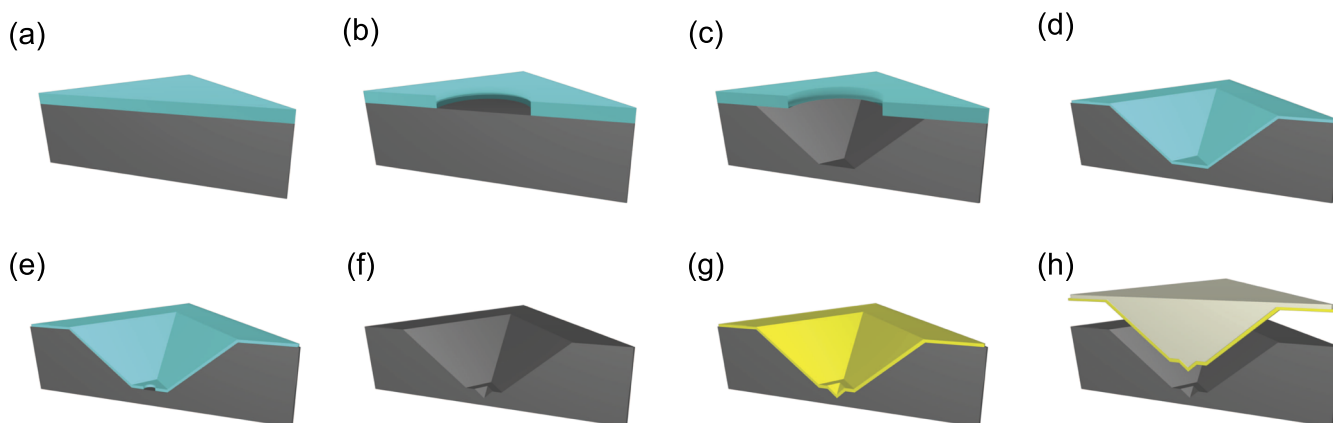


FIG. 2. PTTP's fabrication overview. [(a)–(f)] Steps to generate the segmented cavity template, where the Si substrate and the SiO₂ cover layer are pictured in dark gray and cyan colors, respectively. (g) Au thermal evaporated film (yellow color) deposited over the template. (h) The PTTP is template stripped using an epoxy resin.

This is the crucial step that differs the PTTP method from the conventional micropillar method: the etching process is stopped before finishing the full pyramidal-like cavity, yet with a square bottom of around 1 μm [Fig. 2(c)]. To achieve the correct size, we interrupted the etching process at least three times to investigate the size of the plateau and calculate the actual etching rate in order to predict the final stopping time. After finishing the cavity with a $\sim 1 \mu\text{m}$ square base, a new lithography process takes place [Fig. 2(d)]. For that, a 70 nm thick SiO₂ coating is thermally grown. Afterward, a similar etching process as described above is redone. However, in this additional step, the ion beam lithography exposes Si only over a disk-shaped area of few hundreds of nanometers, centered at the cavity bottom [Fig. 2(e)]. The diameter of the opened area is adjusted to scale the final PTTP nanopillar size. For this second lithography process, the use of FIB is necessary and cannot be substituted by other lithography methods, since the etching structure is smaller than the wavelength of the light. The FIB parameter used was 30 kV of accelerating voltage and ion beam current of 0.1 nA. When compared with the first ion beam lithography process, the FIB current is reduced to improve the resolution of the milling design.

In the following, a second anisotropic etching process is performed with the same parameters used before, but this time it takes just 3 min. The template is finished by removing the SiO₂ cover layer masks with HF solution and cleaning through ultrasonic bath in deionized water and isopropyl alcohol [Fig. 2(f)]. Subsequently, the Si substrate is dried with a stream of N₂. Figures 2(a) and 2(b) show one PTTP template cavity at this fabrication stage. This is the step in which scanning electron microscopy (SEM) is applied to characterize the cavity's morphological structure, since its shape replicates the final PTTP dimensions. Later, the template is coated with a 200 nm Au (99.95%) film by thermal evaporation, as illustrated in Fig. 2(g). Finally, the PTTP is stripped off the cavity using an UV curing epoxy resin [Fig. 2(h)] and fixed at the top of a tuning fork to work as an optical antenna in a shear force AFM-based TERS system. It is important noticing that the template can be properly cleaned and reused to produce more PTTPs without losing quality.

During the first anisotropic etching process, an optical microscope (Axiotech Vario Zeiss) with 50 \times magnification objective was employed to inspect the size of the cavity bottom edge (P), which corresponds to the PTTP probe plateau's size. The inspections were

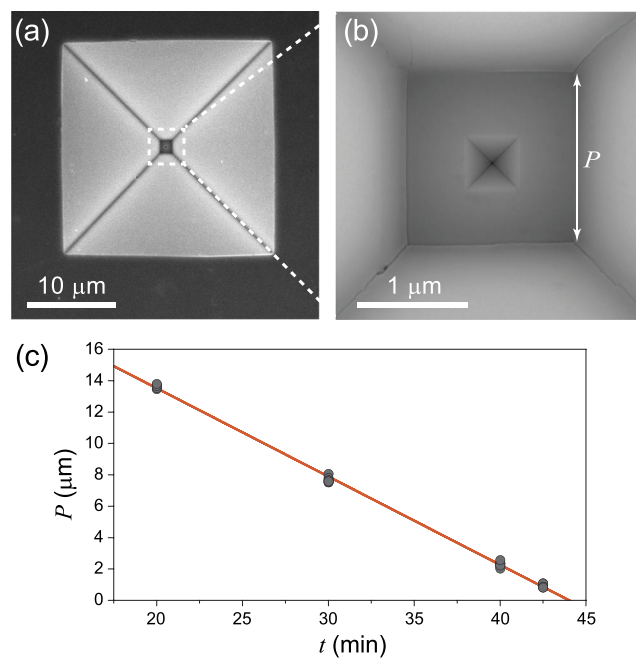


FIG. 3. [(a) and (b)] SEM images of the PTTP's cavity template on the Si substrate. In (b), the white double-arrow shows the characteristic parameter P of the cavity's bottom size, which corresponds to the PTTP plateau's lateral size. (c) Plot of P as a function of the etching time (t) during the first anisotropic etching. Gray circles are the measurements of P by optical microscopy during the etching process. For each step of inspection, seven cavities were randomly chosen for measurements of P . The orange line is the linear fit from which we extracted the etching rate of $P(\mu\text{m}) = 24.8 - 0.56 t(\text{min})$.

made at 20 min, 30 min, and 40 min after the starting point. Another last measurement is taken at around 41 min–43 min, depending on the etching rate. In each inspection, seven cavities were randomly selected to avoid collecting biased data in our statistical analysis. This procedure is essential to calculate the actual etching rate and to predict the final stopping time in order to generate a controlled plateau size of around 1 μm .

Figure 3(c) shows the plot of measurements of the plateau's size (P) during the template fabrication as a function of the etching time (t). We measured seven randomly distributed cavities per inspection step, leading to a deviation of $\Delta P \sim 500$ nm, which is smaller than the optical microscope's lateral resolution. The linear fit (solid line) shows an etching rate of 0.56 $\mu\text{m}/\text{min}$, with respect to the P dimension. This result was used to determine the etching stopping time ($t_{\text{final}} = 42.5$ min), resulting in cavities with a bottom size of ~ 1 μm .

In order to characterize the morphological properties of the template cavities produced, a SEM (FEI Nova NanoLab 600) was used. This includes measuring the nanopillar cavity base edge (L) and the bottom size of the nanopillar cavity (ϕ), which should determine the PTPP apex's diameter [see Fig. 4(a)]. This

measurement was made on 530 PTPP cavities and 185 micropyramid cavities (only the ϕ parameter for the former). The statistical analysis of these parameters is presented in Sec. III A.

C. TERS setup

The TERS experimental setup used in the current work (results shown in Subsection III B) is similar to that described in detail in Refs. 2 and 33. The system is based on an inverted optical microscope (bottom illumination) equipped with an x,y-scan stage for raster-scanning a sample sitting on top of a 0.17 mm thick glass coverslip substrate. A high numerical aperture objective lens (1.4 NA) is used to focus a radially polarized HeNe laser beam ($\lambda_{\text{laser}} = 632.8$ nm) on the substrate's surface. The PTPP is attached to a quartz tuning fork and kept at a distance of ~ 5 nm from the sample's surface by means of a sensitive shear-force feedback mechanism. The scattered field is collected by the same objective (backscattering geometry), passes throughout a low-pass filter that removes the Rayleigh component, and is finally detected by a CCD camera (iDUS -70°C) coupled to a spectrometer (Andor, Shamrock 303i) equipped with a 600 l/mm

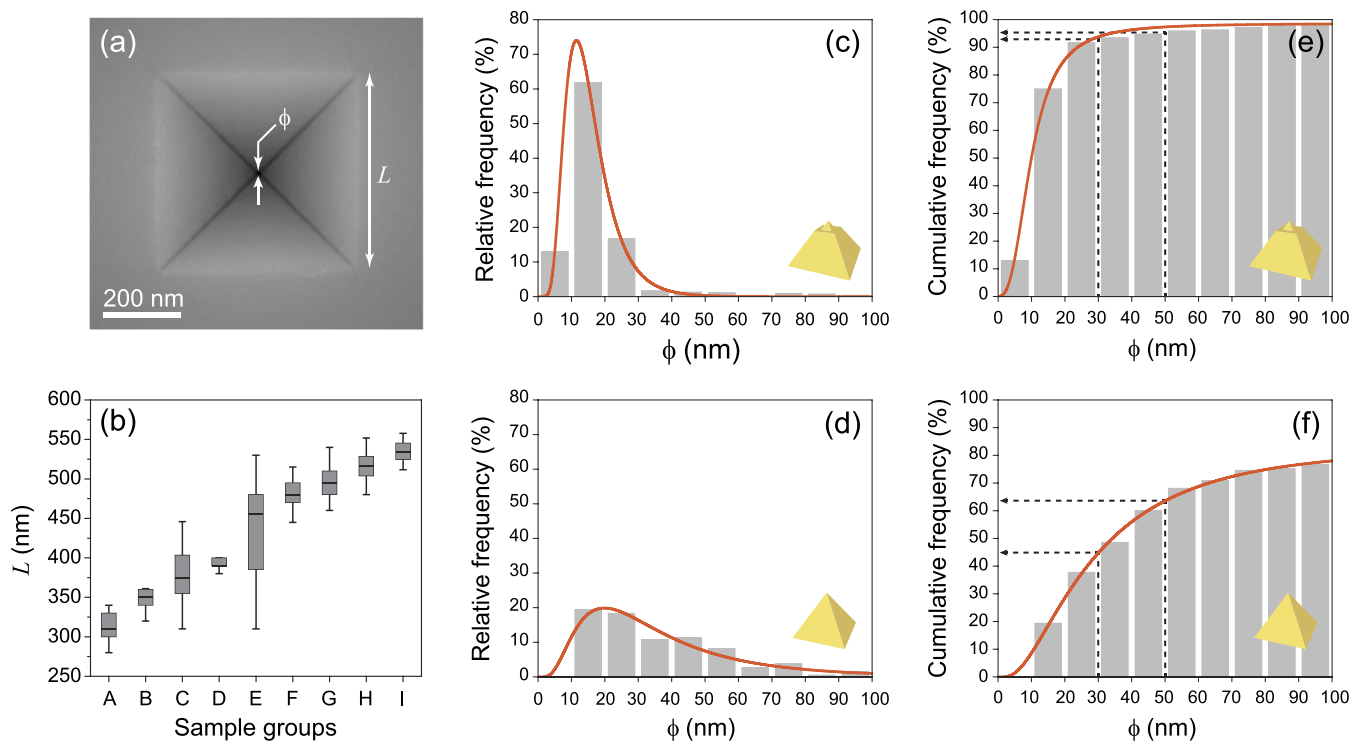


FIG. 4. SEM characterization and statistical analysis of 530 PTPP etched cavities and 185 micropyramid cavities. (a) SEM image of the bottom of a cavity, where the nanopillar cavity and the structural parameters L and ϕ are shown with details. (b) Statistical distribution of L using a box plot representation for nine groups of nanopillar cavities with nominal L values of 310 nm (A), 350 nm (B), 375 nm (C), 390 nm (D), 455 nm (E), 480 nm (F), 500 nm (G), 515 nm (H), and 535 nm (I). The gray boxes represent the interquartile range (IQR)—interval between the first and third quartiles of the distribution (50% of the data). The horizontal black line inside the box indicates the position of the median value of the distribution. The vertical T bars, called whiskers, indicate the minimum and maximum limits for the statistical distribution (no more than $1.0 \times$ IQR from the edge of the box). (c) and (d) are the PTPP and micropyramid cavity bottom size (ϕ) distribution, respectively. The orange curves are log-normal fit of the data, which indicates median values of $\mu = 15$ nm (38 nm) with standard deviations of $\sigma = 7$ nm (28 nm) for the PTPP (micropyramid) fabrication methods. (e) and (f) are the same PTPP and micropyramid cavity bottom size (ϕ) distributions and adjusted curves, but presented in a cumulative frequency plot, where the dashed lines indicate the relative quantity of produced cavities with $\phi < 30$ nm and $\phi < 50$ nm.

grating blazed at 500 nm. For the TERS spectral images acquisition, the laser power at the sample was set to 100 μW , the image pixel size was 20 nm (10 nm), with integration time of 1.5 s (1.0 s) for the first (second) experiment shown in Sec. III B, Fig. 5(b) [Fig. 5(d)]. The tip-down/tip-up spectra shown in Figs. 5(a) and 5(e) were collected with five accumulations of 20 s.

III. RESULTS AND DISCUSSION

A. Statistical analysis of L and ϕ

When compared with the conventional micropillar, or with any other tip that presents field enhancement generated only by the lightning-rod effect, PTTs show a much higher optical efficiency if their second monopole LSPR mode matches the TERS excitation laser's wavelength. This is the reason why L is a critical parameter of a PTT probe, which has to be controlled during fabrication with a maximum variation of 13%, as estimated from the LSPR's quality factor (spectral position divided by the resonance peak width).⁴¹ Here, we performed a statistical analysis of L using data collected from 530 PTTs divided into nine sample groups with nominal target L values of: 310 nm (A), 350 nm (B), 375 nm (C), 390 nm (D), 455 nm (E), 480 nm (F), 500 nm (G), 515 nm (H), and 535 nm (I). Figure 4(b) shows the results obtained using the statistical box plot tool. The variability of the statistical distribution can be easily extracted from the size of the gray box, since the interquartile range is a robust parameter that is not influenced by extreme values with low statistical representativeness. Based on the data shown in Fig. 4(b), the variability around the median value ranged from 2.5% (E group) to 12.5% (D group) in eight out of nine groups, within the acceptable variation range. The E group showed a relatively high variability of 20%, which we assigned to an error that occurs during the FIB milling process of the second lithography mask. In general, the PTT fabrication method generates templates of cavities with narrow variability of the L parameter.

With respect to the ϕ dimension, which measures the final tip's apex and resembles the TERS spatial resolution, 530 PTT cavities and 185 micropillar cavities were analyzed. In general, when the cavity bottom is greater than ~ 10 nm, it shows a unidimensional shape. It happens due to some flaws or damage on the lithography mask, impacting its roundness, which results in a pyramidal-like cavity with a rectangular base, instead of a perfect square base. The difference between the base edges is directly reflected on a unidimensional bottom with approximately the same length.

Figures 4(c) and 4(d) show the ϕ data statistically treated through histograms for PTT cavities and micropillar cavities, respectively. The distribution of ϕ presents a strong tendency toward smaller values, with a clear asymmetry. Thus, a lognormal distribution curve was used to fit the experimental data, showing a median value of $\mu = 15$ nm (38 nm) with a standard deviation of $\sigma = 7$ nm (28 nm) for the PTT (micropillar) fabrication method. Another way to analyze this statistical result is by plotting the same data in a cumulative frequency diagram, as shown in Figs. 4(e) and 4(f) for PTT cavities and micropillar cavities, respectively. The reproducibility of the process is analyzed based on two ranges: $\phi < 30$ nm, considered as the optimum probe apex size, and $\phi < 50$ nm, seen as an acceptable apex size for TERS. The PTT fabrication method generates probes with $\phi < 30$ nm ($\phi < 50$ nm) on 92.4% (95.2%)

of the production batch, whereas the micropillar method leads to probes with $\phi < 30$ nm ($\phi < 50$ nm) on 44.7% (63.6%) of the production batch [see the dashed arrows in Figs. 4(e) and 4(f)].

The clear improvement of the yield of cavities' bottom size smaller than 30 nm can be assigned to the roundness quality of the used lithography mask during the whole micro/nanofabrication process. The micropillar fabrication method is based on the lithography of a disk-shaped region with a diameter of dozens of micrometers, where the Si is exposed, with a subsequent long etching process (dozens of minutes). As a consequence, the formation of H_2 bubbles during the etching process and corrosion power of the KOH solution for a long period of time can lead to small flaws at the mask's edge, especially on its pendent parts. This reflects on a slightly asymmetry of the mask and an increase of the cavity's bottom size after full etching process. On the other hand, the second lithography process of the PTT fabrication method is based on the formation of a disk-shaped region with a diameter of few hundreds of nanometers, and subsequent fast etching process (only 3 min). This downsizing of the lithography process leads to a great improvement in the reproducibility of probes with $\phi < 30$ nm, from 44.7% to 92.4% of yield.

B. TERS performance

To demonstrate the optical performance, we applied three distinct PTTs on a mechanically exfoliated single-layer graphene (SLG) sitting on the glass substrate. This experiment is similar to those previously reported where dozens of PTT probes were utilized.^{12,41,45} The sample presents two distinct regions. The first one is a pristine SLG, used for the evaluation of the spectral enhancement [Fig. 5(a)], whereas the second is a SLG with randomly distributed point defects made using a conventional helium ion microscope, working at 30 kV and low doses ($< 1 \times 10^{12}$ ion/cm²). Details about the modification of graphene using He ions can be found elsewhere.^{50–52} These point defects were used to generate local disorder-induced scattering [Figs. 5(b) and 5(c)].

Although an in-depth description of TERS in two-dimensional systems requires a careful analysis of the field distribution,⁴⁴ conventionally, the optical efficiency of a TERS probe is measured through the spectral enhancement generated when the tip is approached to the sample. This figure-of-merit is given by $F_{\text{TERS}} = I_{\text{tip-down}}/I_{\text{tip-up}}$ ($\approx I_{\text{TERS}}/I_{\text{confocal}}$), where $I_{\text{tip-down}}$ and $I_{\text{tip-up}}$ are the intensities of a given Raman peak with the tip approached and retracted, respectively.^{53,54} Figure 5(a) shows a plot with spectra acquired on the pristine part of the SLG sample with the PTTs (greenish spectra) and without the PTTs (bluish spectra).

The spectral signal enhancement for the first PTT analyzed (PTT#1), with $L = 490$ nm and $\phi = 15$ nm, was measured as $F_{\text{TERS}} = 51$ for the 2D band (centered at ~ 2700 cm⁻¹).⁵⁵ This is around one order of magnitude higher than the spectral enhancements generated by the following conventional TERS probes applied in similar AFM-based TERS setups measuring graphene: gold micropillar ($F_{\text{TERS}} \sim 2.3$ ³⁷ and $F_{\text{TERS}} \sim 3.4$ ⁴¹), electrochemically etched gold tip ($F_{\text{TERS}} \sim 2.1$ ⁵), and commercially available standard cantilever tip covered with a thin silver layer ($F_{\text{TERS}} \sim 8.5$,²⁹ $F_{\text{TERS}} \sim 3.0$,³² $F_{\text{TERS}} \sim 2.2$,²⁷ and $F_{\text{TERS}} \sim 1.5$ ²⁸). Furthermore, this result is in line with previously reported results for PTT probes in similar experiments,

where $F_{\text{TERS}} = 24$ (Ref. 41), $F_{\text{TERS}} = 100$ (Ref. 43), and $F_{\text{TERS}} = 72$ (Ref. 12) were measured.

It is important noticing that the spectral enhancement is impacted by the sample dimension illuminated by the incident laser. For example, the same probe provides larger F_{TERS} from a carbon nanotube (one-dimensional sample) than from a graphene

(two-dimensional sample), because the far-field signal originates from the whole focus area on the graphene case, reducing its near-field to far-field signal ratio.⁴¹ Therefore, a more embracing definition is given by the signal enhancement factor $M_{\text{TERS}} = (F_{\text{TERS}} - 1) \times A_{\text{FF}}/A_{\text{NF}}$, which takes into account roughly the sample's area illuminated by the incident laser (A_{FF}) and

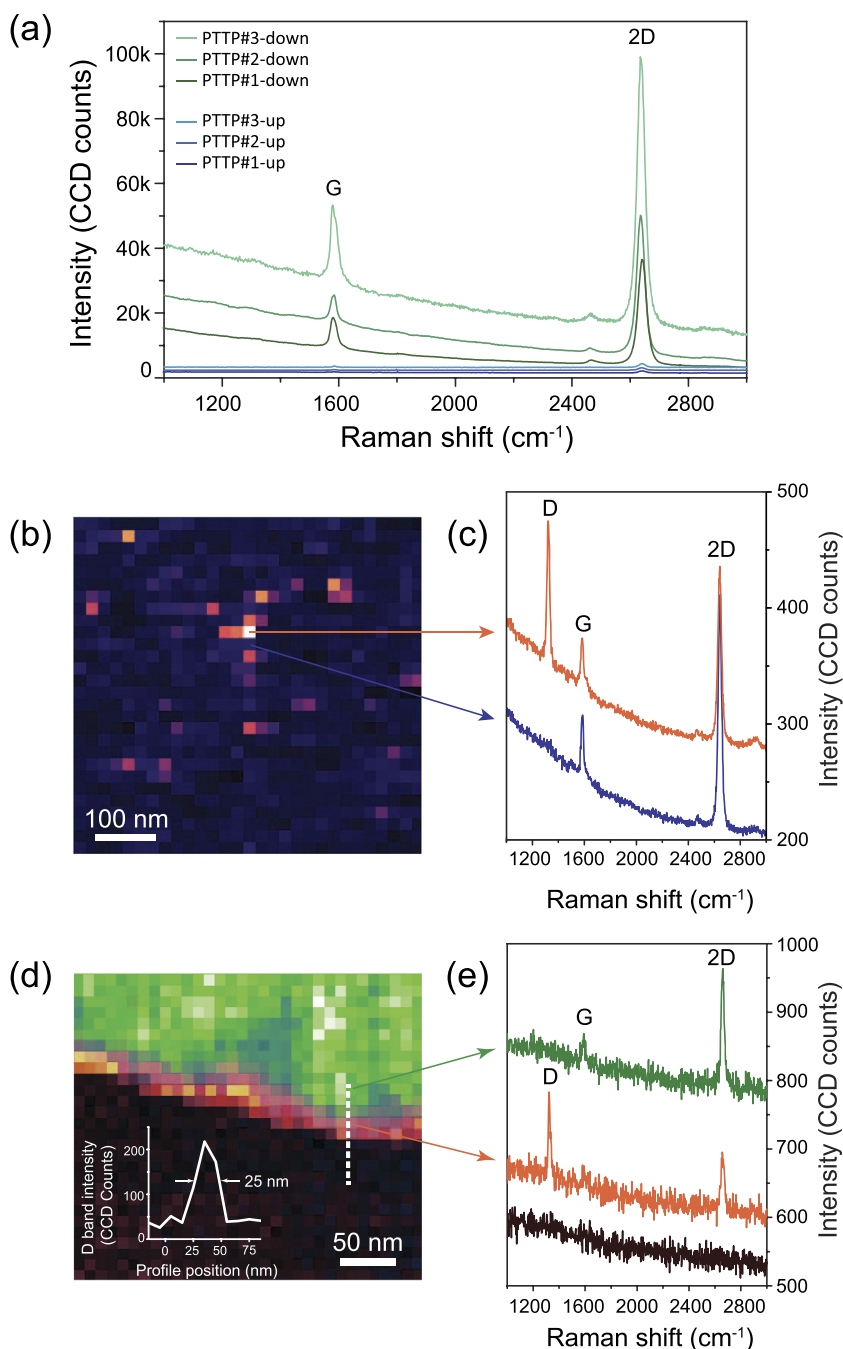


FIG. 5. (a) Raman spectra of an exfoliated single-layer graphene, acquired with the PTP (indicated as tip-down) and without the PTP (indicated as tip-up), for each of the three distinct PTPs, which indicates a 2D band intensity enhancement of $51\times$ for PTP#1, $58\times$ for PTP#2, and $72\times$ for PTP#3. The pair of spectra of PTP#2 and PTP#3 was shifted to clarify. (b) TERS spectral image, made with PTP#1, with a pixel size of 20 nm and a color scale rendering the defect-induced D band ($\sim 1350\text{ cm}^{-1}$) intensity. (c) Raman spectra extracted from the hyperspectral image (b) at pixel positions indicated by the arrows. The orange spectrum was shifted to clarify. (d) and (e) are the results from a TERS experiment using the PTP#3, acquired at the edge region of a pristine graphene sample using a different PTP probe. (d) TERS spectral image with a pixel size of 10 nm, reddish color rendering the defect-induced D band and greenish color rendering the 2D band intensity. The D band intensity profile across the graphene edge (white dashed line) is shown in the figure inset. (e) Raman spectra extracted from the hyperspectral image (d) at pixel positions indicated by the arrows and a dark brown spectrum from pixel position on the glass substrate without graphene. The dark brown and the orange spectra were shifted to clarify.

the probe's apex area (A_{NF}). The PTTP used (PTTP#1) was template stripped from a previously characterized cavity, which showed a bottom size of $\phi = 15$ nm. Thus, we can consider $A_{NF} \approx \pi(15/2)^2$ nm². The laser illumination area can be calculated by considering its wavelength ($\lambda_{laser} = 632.8$ nm) and the oil immersion objective numerical aperture ($NA = 1.4$), leading to $A_{FF} \approx \pi(550/2)^2$ nm². Therefore, we calculated $M = 6.7 \times 10^4$ for this PTTP and reported TERS experiment.

Figure 5(b) shows a TERS spectral image of the SLG region with He-ion induced defects, where the color scale renders the disorder-induced D band (~ 1350 cm⁻¹) intensity.^{50,55} The experiment was performed using the same PTTP#1 and an incident laser power of ~ 100 μ W, measured before the objective lens. The point defects present spectral features clearly distinct from that obtained from the pristine positions, as shown in Fig. 5(c). The former [orange spectrum in Fig. 5(c)] shows a strong D peak and a weaker 2D peak when compared to that acquired at the pristine position (blue spectrum). Moreover, we can estimate the image resolution to be smaller than the pixel size (20 nm), corroborating with the template cavity measurements ($\phi = 15$ nm). Interestingly, this near-field image indicates a defect density of ~ 61 μ m⁻² and an average distance among defects of $L_D \approx 130$ nm. We compared these measured values to the ones extracted from the spectrum (not shown) acquired on the same sample position and without the PTTP (far field spectrum). By applying the protocol described in Ref. 56, we measured G band's linewidth of $\Gamma_G = 17.6$ cm⁻¹, and $(A_D/A_G) \times E_{laser}^4 = 1.37$ (eV⁴), where A_D and A_G are the areas under the Lorentzian curves that adjust the D and G band peaks, and E_{laser} is the incident laser energy. Based on the diagram for the contribution of point-like defects to the far-field Raman spectrum,⁵⁶ we would expect $L_D > 100$ nm, corroborating with our findings.

The optical efficiency was also measured for the two other PTTPs using the same criteria. The 2D band intensity enhancement for PTTP#2, with $L = 510$ nm and $\phi = 20$ nm, was measured as $F_{TERS} = 58$, and for PTTP#3, with $L = 480$ nm and $\phi = 20$ nm, $F_{TERS} = 72$. Their signal enhancement factors were calculated as $M = 4.3 \times 10^4$ for PTTP#2 and $M = 5.4 \times 10^4$ for PTTP#3. Finally, following a more traditional way of measuring the TERS spatial resolution, we performed a TERS experiment using PTTP#3 near the edge region of a pristine SLG. Figure 5(d) shows a TERS spectral image with a pixel size of 10 nm, in which the reddish color scale renders the disorder-induced D band intensity and the greenish color rendering the 2D band intensity. To measure the spatial resolution, we evaluated the D band intensity profile across the graphene edge [Fig. 5(d) inset], which shows a FWHM of around 25 nm. If we subtract the spatial extent of the D band ($L_d \sim 4$ nm⁵⁷), we conclude that the image resolution is around 20 nm, which corroborates with the previous SEM measurement of the PTTP#3 template's cavity.

IV. CONCLUSION

In summary, we have presented in detail the template stripped-based fabrication process of PTTP probes, highlighting its distinction from the micropylramids method. Based on a statistical analysis of data collected from 530 PTTP cavity templates and 185 micropylramid cavity templates, we have shown that the PTTP method generates probes with an apex diameter smaller than 30 nm in 92.4%

of the batch, a substantial yield improvement when compared to the micropylramid method, where $\phi < 30$ nm was obtained for 44.7% of the cavities. The explanation for that level of improvement is based on the downscaling of the lithography mask used in the fabrication process, going from few dozens of micrometers for the micropylramids method to few hundreds of nanometers for the PTTP method.

In addition, we also analyzed the PTTP's nanopylramid edge size, a critical parameter for LSPR spectral tuning. We have shown that the variability of L was typically smaller than 12.5%, compatible with its plasmon resonant quality factor ($Q \approx 10$). Therefore, the PTTP fabrication method not just results in a unique design capable of generating tunable monopole LSPR modes but it also proved to be an improvement in terms of reproducibility and batch production.

To check its actual optical performance, three PTTPs were tested in a TERS experiment performed on a graphene sample. The results indicate signal enhancement factors ($M_{TERS} = 6.7 \times 10^4$, $M_{TERS} = 4.3 \times 10^4$, and $M_{TERS} = 5.4 \times 10^4$) at least one order of magnitude higher than those archived by a conventional gold micropylramid and other conventional TERS probes.^{41,57} In addition, the image resolution was measured for two of these PTTPs through two distinct experiments. In the first one, the TERS image of randomly distributed point defects generated by He-ion bombardment on SLG indicating a spatial resolution better than 20 nm. In the second experiment, the D band line width at the graphene edge suggested a spatial resolution of around 20 nm, both in line with the template cavity SEM analysis.

ACKNOWLEDGMENTS

The authors acknowledge financial support from Inmetro, CNPq (Grant Nos. 309537/2019-3, 429165/2018-8, 302775/2018-8, 305881/2019-1, and 436381/2018-4), FINEP (Grant Nos. 01.13.0330.00 and 01.13.0357.00), SisNANO, MCTI Sibratec-Nano, INCT Nanomateriais de Carbono, CAPES-PROBRAL (Grant No. 88881.198744/2018-01), FAPEMIG (Grant No. APQ-01361-14), and FAPERJ.

DATA AVAILABILITY

The data that support the findings of this study are available from the corresponding author upon reasonable request.

REFERENCES

1. L. Novotny and B. Hecht, *Principles of Nano-Optics* (Cambridge University Press, 2012).
2. L. G. Cançado, A. Hartschuh, and L. Novotny, *J. Raman Spectrosc.* **40**, 1420 (2009).
3. B.-S. Yeo, J. Stadler, T. Schmid, R. Zenobi, and W. Zhang, *Chem. Phys. Lett.* **472**, 1 (2009).
4. L. Novotny and N. Van Hulst, *Nat. Photonics* **5**, 83 (2011).
5. T. L. Vasconcelos, B. S. Archanjo, B. Fragneaud, B. S. Oliveira, J. Riikonen, C. Li, D. S. Ribeiro, C. Rabelo, W. N. Rodrigues, A. Jorio, C. A. Achete, and L. G. Cançado, *ACS Nano* **9**, 6297 (2015).
6. T. Deckert-Gaudig, A. Taguchi, S. Kawata, and V. Deckert, *Chem. Soc. Rev.* **46**, 3922 (2017).
7. F. Shao and R. Zenobi, *Anal. Bioanal. Chem.* **411**, 37 (2019).

- ⁸Z. He, Z. Han, M. Kizer, R. J. Linhardt, X. Wang, A. M. Sinyukov, J. Wang, V. Deckert, A. V. Sokolov, J. Hu *et al.*, *J. Am. Chem. Soc.* **141**, 753 (2018).
- ⁹P. Z. El-Khoury and E. Aprà, *J. Phys. Chem. C* **124**, 17211 (2020).
- ¹⁰P. Muehlschlegel, H.-J. Eisler, O. J. Martin, B. Hecht, and D. Pohl, *Science* **308**, 1607 (2005).
- ¹¹N. Mauser and A. Hartschuh, *Chem. Soc. Rev.* **43**, 1248 (2014).
- ¹²T. L. Vasconcelos, B. S. Archanjo, B. S. Oliveira, W. F. Silva, R. S. Alencar, C. Rabelo, C. A. Achete, A. Jorio, and L. G. Cançado, *IEEE J. Sel. Top. Quantum Electron.* **27**, 4600411 (2020).
- ¹³M. Richard-Lacroix, Y. Zhang, Z. Dong, and V. Deckert, *Chem. Soc. Rev.* **46**, 3922 (2017).
- ¹⁴S. F. Becker, M. Esmann, K. Yoo, P. Gross, R. Vogelgesang, N. Park, and C. Lienau, *ACS Photonics* **3**, 223 (2016).
- ¹⁵L. Langelüddecke, P. Singh, and V. Deckert, *Appl. Spectrosc.* **69**, 1357 (2015).
- ¹⁶X. Shi, N. Coca-López, J. Janik, and A. Hartschuh, *Chem. Rev.* **117**, 4945 (2017).
- ¹⁷S. Jiang, X. Zhang, Y. Zhang, C. Hu, R. Zhang, Y. Zhang, Y. Liao, Z. J. Smith, Z. Dong, and J. G. Hou, *Light: Sci. Appl.* **6**, e17098 (2017).
- ¹⁸N. Hayazawa, Y. Inouye, Z. Sekkat, and S. Kawata, *Opt. Commun.* **183**, 333 (2000).
- ¹⁹N. Hayazawa, T. Yano, H. Watanabe, Y. Inouye, and S. Kawata, *Chem. Phys. Lett.* **376**, 174 (2003).
- ²⁰B. Ren, G. Picardi, and B. Pettinger, *Rev. Sci. Instrum.* **75**, 837 (2004).
- ²¹B. Pettinger, B. Ren, G. Picardi, R. Schuster, and G. Ertl, *Phys. Rev. Lett.* **92**, 096101 (2004).
- ²²S.-Y. Ding, J. Yi, J.-F. Li, B. Ren, D.-Y. Wu, R. Panneerselvam, and Z.-Q. Tian, *Nat. Rev. Mater.* **1**, 16021 (2016).
- ²³R. M. Stöckle, Y. D. Suh, V. Deckert, and R. Zenobi, *Chem. Phys. Lett.* **318**, 131 (2000).
- ²⁴P. Verma, *Chem. Rev.* **117**, 6447 (2017).
- ²⁵B. Pettinger, P. Schambach, C. J. Villagómez, and N. Scott, *Annu. Rev. Phys. Chem.* **63**, 379 (2012).
- ²⁶J. Stadler, T. Schmid, and R. Zenobi, *ACS Nano* **5**, 8442 (2011).
- ²⁷W. Su and D. Roy, *J. Vac. Sci. Technol., B* **31**, 041808 (2013).
- ²⁸S. Mignuzzi, N. Kumar, B. Brennan, I. S. Gilmore, D. Richards, A. J. Pollard, and D. Roy, *Nanoscale* **7**, 19413 (2015).
- ²⁹W. Su, N. Kumar, N. Dai, and D. Roy, *Chem. Commun.* **52**, 8227 (2016).
- ³⁰M. Rahaman, R. D. Rodriguez, G. Plechinger, S. Moras, C. Schüller, T. Korn, and D. R. T. Zahn, *Nano Lett.* **17**, 6027 (2017).
- ³¹R. Beams, *J. Raman Spectrosc.* **49**, 157 (2018).
- ³²X. Li, Y. Liu, Z. Zeng, P. Wang, Y. Fang, and L. Zhang, *Spectrochim. Acta, Part A* **190**, 378 (2018).
- ³³C. Rabelo, H. Miranda, T. L. Vasconcelos, L. G. Cançado, and A. Jorio, in *2019 4th International Symposium on Instrumentation Systems, Circuits and Transducers (INSCIT)* (IEEE, 2019), pp. 1–6.
- ³⁴R. Kato, T. Umakoshi, R. T. Sam, and P. Verma, *Appl. Phys. Lett.* **114**, 073105 (2019).
- ³⁵R. S. Alencar, C. Rabelo, H. L. S. Miranda, T. L. Vasconcelos, B. S. Oliveira, A. Ribeiro, B. C. Públio, J. Ribeiro-Soares, A. G. S. Filho, L. G. Cançado, and A. Jorio, *Nano Lett.* **19**, 7357 (2019).
- ³⁶C. Rabelo, T. Vasconcelos, B. S. Oliveira, H. Miranda, L. G. Cançado, and A. Jorio, *Phys. Rev. Appl.* **14**, 024056 (2020).
- ³⁷T. W. Johnson, Z. J. Lapin, R. Beams, N. C. Lindquist, S. G. Rodrigo, L. Novotny, and S.-H. Oh, *ACS Nano* **6**, 9168 (2012).
- ³⁸J. Henzie, E.-S. Kwak, and T. W. Odom, *Nano Lett.* **5**, 1199 (2005).
- ³⁹P. Nagpal, N. C. Lindquist, S.-H. Oh, and D. J. Norris, *Science* **325**, 594 (2009).
- ⁴⁰N. C. Lindquist, P. Nagpal, A. Lesuffleur, D. J. Norris, and S.-H. Oh, *Nano Lett.* **10**, 1369 (2010).
- ⁴¹T. L. Vasconcelos, B. S. Archanjo, B. S. Oliveira, R. Valaski, R. C. Cordeiro, H. G. Medeiros, C. Rabelo, A. Ribeiro, P. Ercius, C. A. Achete, A. Jorio, and L. G. Cançado, *Adv. Opt. Mater.* **6**, 1800528 (2018).
- ⁴²B. S. Archanjo, T. L. Vasconcelos, B. S. Oliveira, C. Song, F. I. Allen, C. A. Achete, and P. Ercius, *ACS Photonics* **5**, 2834 (2018).
- ⁴³H. Miranda, C. Rabelo, T. L. Vasconcelos, L. G. Cançado, and A. Jorio, *Phys. Status Solidi RRL* **14**(9), 2000212 (2020).
- ⁴⁴H. Miranda, C. Rabelo, L. G. Cançado, T. L. Vasconcelos, B. S. Oliveira, F. Schulz, H. Lange, S. Reich, P. Kusch, and A. Jorio, *Phys. Rev. Res.* **2**, 023408 (2020).
- ⁴⁵A. C. Gadelha, D. A. Ohlberg, C. Rabelo, E. G. Neto, T. L. Vasconcelos, J. L. Campos, J. S. Lemos, V. Ornelas, D. Miranda, R. Nadas *et al.*, *arXiv:2006.09482* (2020).
- ⁴⁶H. Seidel, L. Csepregi, A. Heuberger, and H. Baumgärtel, *J. Electrochem. Soc.* **137**, 3612 (1990).
- ⁴⁷I. Barycka and I. Zobel, *Sens. Actuators, A* **48**, 229 (1995).
- ⁴⁸M. Jin, V. Pully, C. Otto, A. van den Berg, and E. T. Carlen, *J. Phys. Chem. C* **114**, 21953 (2010).
- ⁴⁹H. Seidel, L. Csepregi, A. Heuberger, and H. Baumgärtel, *J. Electrochem. Soc.* **137**, 3626 (1990).
- ⁵⁰M. M. Lucchese, F. Stavale, E. H. M. Ferreira, C. Vilani, M. V. O. Moutinho, R. B. Capaz, C. A. Achete, and A. Jorio, *Carbon* **48**, 1592 (2010).
- ⁵¹B. S. Archanjo, A. P. M. Barboza, B. R. A. Neves, L. M. Malard, E. H. M. Ferreira, J. C. Brant, E. S. Alves, F. Plentz, V. Carozo, B. Fragneaud *et al.*, *Nanotechnology* **23**, 255305 (2012).
- ⁵²B. S. Archanjo, B. Fragneaud, L. Gustavo Cançado, D. Winston, F. Miao, C. Alberto Achete, and G. Medeiros-Ribeiro, *Appl. Phys. Lett.* **104**, 193114 (2014).
- ⁵³J. Stadler, T. Schmid, and R. Zenobi, *Nanoscale* **4**, 1856 (2012).
- ⁵⁴A. R. Neto, C. Rabelo, L. G. Cançado, M. Engel, M. Steiner, and A. Jorio, in *2019 4th International Symposium on Instrumentation Systems, Circuits and Transducers (INSCIT)* (IEEE, 2019), pp. 1–6.
- ⁵⁵A. Jorio, M. S. Dresselhaus, R. Saito, and G. Dresselhaus, *Raman Spectroscopy in Graphene Related Systems* (John Wiley & Sons, 2011).
- ⁵⁶L. G. Cançado, M. G. Da Silva, E. H. M. Ferreira, F. Hof, K. Kampioti, K. Huang, A. Pénicaud, C. A. Achete, R. B. Capaz, and A. Jorio, *2D Mater.* **4**, 025039 (2017).
- ⁵⁷R. Beams, L. G. Cançado, S.-H. Oh, A. Jorio, and L. Novotny, *Phys. Rev. Lett.* **113**, 186101 (2014).